

Rank-Factorized Implicit Neural Bias: Scaling Super-Resolution Transformer with FlashAttention

Dongheon Lee, Seokju Yun, Jaegyun Im, and Youngmin Ro*

Machine Intelligence Laboratory, University of Seoul, Korea
{dslisleedh, wsz871, imij0522, youngmin.ro}@uos.ac.kr

Code: <https://github.com/dslisleedh/SST>

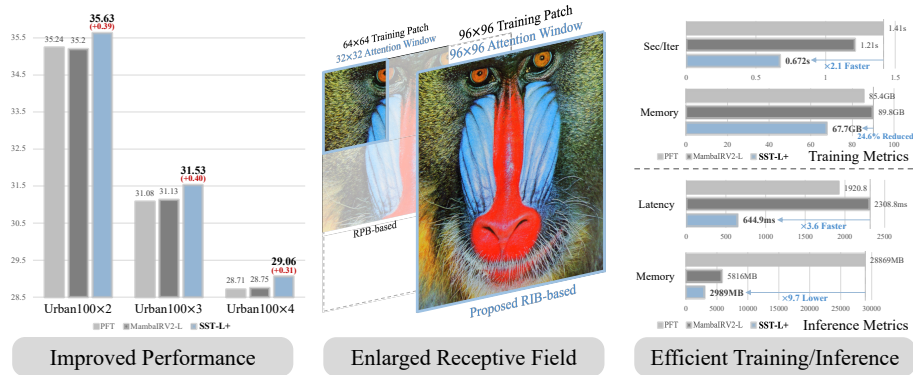


Fig. 1: Overview of our contributions. We enable FlashAttention for Super-Resolution (SR) Transformers by replacing the commonly used relative positional bias (RPB) with our proposed Rank-factorized Implicit Neural Bias (RIB). The resulting efficiency allows us to scale up the SR Transformer significantly, including the self-attention window size and training patch size up to 96×96 , and also datasets from DF2K to DFLIP. Consequently, our network achieves remarkable performance while drastically reducing training/inference costs.

Abstract. Recent Super-Resolution (SR) methods mainly adopt Transformers for their strong long-range modeling capability and exceptional representational capacity. However, most SR Transformers rely heavily on relative positional bias (RPB), which prevents them from leveraging hardware-efficient attention kernels such as FlashAttention. This limitation imposes a prohibitive computational burden during both training and inference, severely restricting attempts to scale SR Transformers by enlarging the training patch size or the self-attention window. Consequently, unlike other domains that actively exploit the inherent scalability of Transformers, SR Transformers remain heavily focused on

* Corresponding author

effectively utilizing limited receptive fields. In this paper, we propose Rank-factorized Implicit Neural Bias (RIB), an alternative to RPB that enables FlashAttention in SR Transformers. Specifically, RIB approximates positional bias using low-rank implicit neural representations and concatenates them with pixel content tokens in a channel-wise manner, turning the element-wise bias addition in attention score computation into a dot-product operation. Further, we introduce a convolutional local attention and a cyclic window strategy to fully leverage the advantages of long-range interactions enabled by RIB and FlashAttention. We enlarge the window size up to 96×96 while jointly scaling the training patch size and the dataset size, maximizing the benefits of Transformers in the SR task. As a result, our network achieves **35.63 dB PSNR** on Urban100 $\times 2$, while reducing training and inference time by **2.1 \times** and **2.9 \times** , respectively, compared to the RPB-based SR Transformer (PFT).

Keywords: Super-Resolution · FlashAttention · Implicit Neural Field

1 Introduction

Super-Resolution (SR) aims to reconstruct a high-resolution (HR) image from a low-resolution (LR) input and has long been a fundamental problem in computer vision. Modeling long-range dependencies is crucial for SR, as distant but correlated patterns, such as repeated textures and edges, can help disambiguate the inherently ill-posed LR inputs. Accordingly, Transformers [58] have recently emerged as a promising architecture for SR tasks because their core operator, self-attention, enables long-range interactions and input-adaptive feature aggregation, offering strong representational capacity.

However, adopting Transformers for SR in practice still faces several limitations that prevent the full leverage of its powerful representational capability: (i) *The quadratic cost of self-attention* in the number of tokens makes global attention prohibitively expensive for high-resolution feature maps that consist of pixel-level tokens without a patchify stem. As a result, many SR Transformers resort to window-based attention with relatively small windows [32, 35], which restricts the capturing of long-range dependencies across distant but correlated regions. (ii) *Most methods are limited to training on small cropped patches* (e.g., 64×64), since leveraging larger patches (e.g., 96×96) substantially increases the training budget, although the richer global context can improve performance [30, 31, 62]. (iii) *Many SR Transformers are still trained on relatively small datasets* such as DF2K [1, 57] (3,450 images), despite the availability of much larger datasets like LSDIR [31] (84,991 images) and DiverSeg-IP [42] (526,503 images). Data scaling has driven substantial gains for Transformers in other vision domains [3, 16, 27, 43].

Currently, many SR methods primarily mitigate the limitation (i), while the orthogonal gains from limitations (ii) and (iii) remain underexplored. We identify SR Transformers’ heavy reliance on Relative Positional Bias (RPB) as the hidden bottleneck underlying this research trend. RPB injects a strong spatial

prior into self-attention by adding a learnable, distance-dependent bias to the attention logits ($\mathbf{S} = \mathbf{Q}\mathbf{K}^\top$), and is crucial for SR performance. Yet, incorporating RPB typically requires either materializing the score matrix or performing additional indexing and memory reads, making it difficult to use with hardware-efficient self-attention kernels (e.g., FlashAttention [11, 12, 49]), which aim to reduce memory I/O and to avoid materializing the score matrix. This incompatibility forces existing models to rely on slow, memory-intensive implementations, which in turn hinders the effective scaling of training patch size and data. Consequently, instead of pursuing scalability, previous works have been largely confined to designing complex windowing strategies [7, 8, 67, 69] or sub-quadratic alternatives, such as linear-complexity attention [6, 7, 65, 69], Mamba [21, 22, 74], and sparse operators [36], to bypass this efficiency wall.

In this paper, we propose **Rank-factorized Implicit Neural Bias** (RIB), a FlashAttention-compatible alternative to conventional RPB, unlocking the window limits for SR Transformers. Specifically, RIB parameterizes positional bias into two low-rank implicit neural representations ($\mathbf{Q}_p, \mathbf{K}_p \in \mathbb{R}^{N \times R}$) generated by a coordinate-based multi-layered perceptron (MLP). Then, resulting spatial priors are injected to self-attention by concatenating them to tokens predicted from pixel contents ($\mathbf{Q}_c, \mathbf{K}_c \in \mathbb{R}^{N \times D}$), thereby memory-efficiently emulating the element-wise bias addition through dot-products (e.g., $[\mathbf{Q}_c, \mathbf{Q}_p][\mathbf{K}_c, \mathbf{K}_p]^\top = \mathbf{Q}_c\mathbf{K}_c^\top + \mathbf{Q}_p\mathbf{K}_p^\top$). This novel design separates the number of bias parameters from the window size and remains compatible with any FlashAttention implementation, unlike traditional RPB. Moreover, compared to Rotary Positional Embedding (RoPE) [23, 53], which injects spatial prior via rotating \mathbf{Q}_c and \mathbf{K}_c , RIB explicitly decouples the pixel contents and spatial prior, thereby preserving the integrity of pixel-content representations. Finally, to better exploit the larger window self-attention enabled by our RIB and FlashAttention, we propose a Convolutional Local Attention (CLA) to focus self-attention on a larger context and a cyclic window strategy that periodically expands the attention window to balance long-range interaction and multi-scale feature extraction.

Building on our proposals, we introduce a FlashAttention-accelerated SR Transformer, dubbed **Scalable SR Transformer** (SST). With a 64×64 attention window, SST achieves +0.16 dB PSNR on Urban100 \times 2 over HAT, despite using only 12M parameters compared to HAT’s 20M. We further present SST+, which scales both the attention window and the training patch size up to 96×96 . Even with 8M fewer parameters, it attains +0.18 dB higher PSNR than ATD on Urban100 \times 2, which is also trained on 96×96 patches. Finally, by scaling the model to 20M parameters and training on the substantially larger DFLIP datasets, which consist of DIV2K, Flickr2K, LSDIR-train, and DiverSeg-IP, instead of the commonly used DF2K, we obtain a striking result: +0.4 dB PSNR on Urban100 \times 3 over prior state-of-the-art (SOTA) methods trained under the same setting. Beyond notable performance improvements, our method is markedly more efficient. While leveraging 96×96 attention windows and training patches, it delivers $2.1\times$ faster training with 24.6% lower memory than prior methods trained with 64×64 patches. At inference time, it achieves $3.6\times$ lower latency

and $9.7\times$ less memory usage. Detailed ablation studies verify that each proposed component contributes to these gains and delivers substantial efficiency gains, while visual analyses show that our approach not only restores visually pleasing outputs but also effectively leverages a larger receptive field.

In summary, by making FlashAttention practical for SR Transformers and fully exploiting the resulting scalability, we achieve substantial efficiency gains and translate them into powerful performance, highlighting large-context and large-data scaling as a promising research direction, as shown in Figure 1.

2 Preliminaries

In this section, we briefly review the key components relevant to our method, including general SR architectures, SR Transformers, window-based self-attention, positional bias, and FlashAttention.

2.1 SR Architecture

A typical SR architecture adopts a residual-in-residual design [71] composed of a shallow feature extractor (\mathcal{E}_s), a deep feature extractor (\mathcal{E}_d), and an upsampler (\mathcal{U}), as illustrated in Figure 2 (a). The \mathcal{E}_s is a 3×3 convolution that maps an input LR image $I_{LR} \in \mathbb{R}^{H \times W \times 3}$, where H and W denote the height and width of I_{LR} , respectively, to shallow features $F_s \in \mathbb{R}^{H \times W \times D}$, where D is the base channel dimension. The \mathcal{E}_d , instantiated with chosen core operators such as convolution [33], self-attention [32], or Mamba [22], takes F_s as input and predicts deep features $F_d \in \mathbb{R}^{H \times W \times D}$. Finally, the \mathcal{U} receives $F \in \mathbb{R}^{H \times W \times D}$, obtained by element-wise addition of F_s and F_d , and outputs the reconstructed image $I_{SR} \in \mathbb{R}^{rH \times rW \times 3}$, where r denotes the upscaling factor. Some prior studies further employ an image-wise skip connection [17, 30]; similarly, we add a nearest-neighbor interpolated I_{LR} to the \mathcal{U} 's output, treating the \mathcal{U} as a residual image predictor [26].

2.2 SR Transformers and Window-based Self-attention

Transformers leverage self-attention to model long-range dependencies from token features $X \in \mathbb{R}^{B \times N \times D}$, where N denotes the number of tokens. Unlike high-level vision tasks that typically tokenize image patches into tokens (e.g., 16×16 patches in ViT) [16], SR commonly treats each pixel as a token to preserve pixel-wise fidelity, leading to a much larger $N = HW$. To clarify the computational bottleneck induced by pixel-level tokenization, we briefly review scaled dot-product self-attention, considering only a single head. Self-attention projects X into queries, keys, and values: $\mathbf{Q} = X\mathbf{W}_q$, $\mathbf{K} = X\mathbf{W}_k$, and $\mathbf{V} = X\mathbf{W}_v$, where $\mathbf{W}_q, \mathbf{W}_k, \mathbf{W}_v \in \mathbb{R}^{D \times D}$. It then computes the scaled similarity matrix $\mathbf{S} = \mathbf{Q}\mathbf{K}^T / \sqrt{D} \in \mathbb{R}^{B \times N \times N}$, applies SoftMax along the token dimension to obtain attention weights $\mathbf{P} = \text{SoftMax}(\mathbf{S}) \in \mathbb{R}^{B \times N \times N}$, and aggregates values as $\mathbf{O} = \mathbf{P}\mathbf{V} \in \mathbb{R}^{B \times N \times D}$.

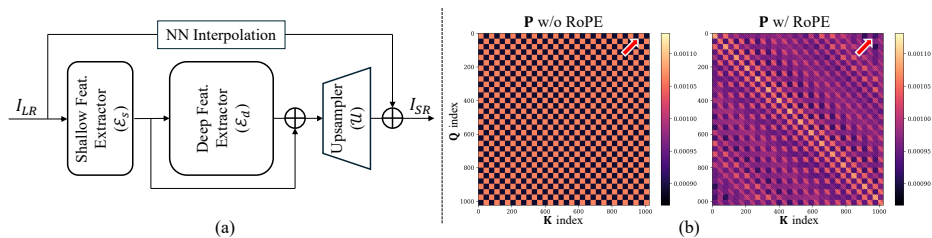


Fig. 2: Preliminaries and motivation. (a) Overview of the general SR architecture. (b) Comparison of the attention probability matrix $\mathbf{P} = \text{SoftMax}(\mathbf{Q}\mathbf{K}^\top/\sqrt{D})$ with (right) and without (left) RoPE [23]. For intuition, \mathbf{P} is computed in a toy setting where $\mathbf{Q} = \mathbf{K}$ is obtained by sampling random two orthogonal 32-dimensional vectors and spatially tiling them to form a 32×32 feature map. Typical SR Transformers set D to 30 [5, 32, 76]. With RoPE, similarity between repeated patterns becomes unstable and often attenuates as the spatial offset increases, or vice versa, due to phase-wrapping effects, as highlighted by the red arrow.

This input-adaptive global aggregation provides strong representational power, but incurs quadratic computational/memory complexity $O(N^2D)$. Moreover, the aforementioned pixel-level tokenization makes global attention prohibitively expensive due to the large number of tokens. For example, a ViT with a 224×224 input and 16×16 patches processes $N = (224/16)^2 = 196$ tokens, whereas a $\times 2$ SR Transformer for a 1280×720 output takes a 640×360 LR input and processes $N = 640 \times 360 = 230,400$ tokens. As a result, most SR Transformers adopt window-based self-attention, computing attention only within local $M \times M$ windows (e.g., $M \in \{8, 16, 32\}$), which reduces complexity to $O(NM^2D)$. While this windowing strategy substantially improves efficiency, it also limits direct long-range interactions, leaving SR Transformers to balance computational cost against long-range modeling.

2.3 FlashAttention and Positional Bias

In language modeling tasks [18, 63], where models must process huge numbers of tokens, hardware-efficient attention kernels such as FlashAttention [11, 12, 49] are widely used to mitigate the memory bottlenecks of long-context self-attention. Technically, FlashAttention improves both memory usage and runtime by using IO-aware tiling and kernel fusion to compute exact self-attention without materializing the full $N \times N$ matrices (\mathbf{S} and \mathbf{P}), thereby notably reducing memory traffic. These optimizations significantly accelerate both training and inference speed compared to the standard implementations, and have been instrumental in scaling Transformers.

However, FlashAttention cannot be directly applied to many SR Transformers due to the use of RPB [35, 47], which provides a strong spatial prior and often yields notable performance gains. Specifically, RPB adds a distance-dependent bias matrix $\mathbf{B} \in \mathbb{R}^{1 \times N \times N}$ to the attention logits, i.e., $\hat{\mathbf{S}} = \mathbf{S} + \mathbf{B}$. Therefore,

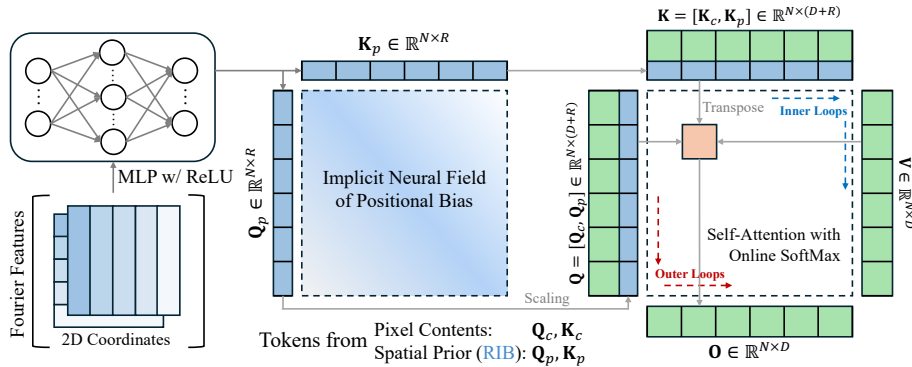


Fig. 3: Overall illustration for proposed Rank-factorized Implicit Neural Bias (RIB).

incorporating RPB either requires explicitly materializing an additional $N \times N$ matrix or performing extra memory accesses and indexing into a bias table to add the corresponding biases [15, 30]. Such operations break the assumptions behind many fused FlashAttention kernels, and therefore are not supported in a large portion of existing FlashAttention implementations.

In contrast, modern Large Language Models (LLMs) often adopt a RoPE [53], which is fully compatible with FlashAttention. RoPE injects positional prior by applying distance-dependent rotations to \mathbf{Q} and \mathbf{K} , so that relative phase differences are reflected during the dot-product computation of \mathbf{S} . Since RoPE does not require materializing or adding an extra $N \times N$ bias, RoPE can be seamlessly used with FlashAttention kernels, and recent works have also explored its adaptation to vision transformers [23]. Nevertheless, as illustrated in Figure 2 (b), RoPE can substantially weaken similarities between repeated patterns at large spatial offsets, which is crucial for the SR task, due to phase wrap/aliasing especially under small head dimensions (e.g., ≈ 32). Moreover, since RoPE injects positional information by directly modulating the dot-product with rotated \mathbf{Q}/\mathbf{K} , the positional effect is entangled with the pixel contents. Consequently, compensating for undesired distance-dependent suppression may require altering the \mathbf{Q}/\mathbf{K} content representations themselves, consuming fitting capacity and potentially degrading performance. This motivates us to introduce a FlashAttention-compatible bias that explicitly decouples the spatial prior from the pixel content, similar to the RPB.

3 Proposed Methods

In this section, we describe our proposed methods, including a Rank-factorized Implicit Neural Bias (RIB), a Convolutional Local Attention (CLA), and a cyclic window strategy.

3.1 Rank-factorized Implicit Neural Bias

The main goal of the proposed RIB is to provide a positional bias for self-attention that explicitly disentangles pixel content from spatial priors, while remaining fully compatible with FlashAttention. To this end, we parameterize positional bias using per-token 2D coordinates and their Fourier features. Specifically, given a window with N tokens, we assign each token a normalized 2D coordinate $\mathbf{x} \in [-1, 1]^{N \times 2}$. We augment these coordinates with a Fourier feature mapping [41] to obtain the coordinate embedding $\mathbf{r}_{\text{in}} \in \mathbb{R}^{N \times (2+4L)}$, which is defined as:

$$\mathbf{r}_{\text{in}} = \gamma(\mathbf{x}) = \left[\mathbf{x}, \sin(2^0 \mathbf{x}), \cos(2^0 \mathbf{x}), \dots, \sin(2^{L-1} \mathbf{x}), \cos(2^{L-1} \mathbf{x}) \right], \quad (1)$$

where $[\cdot]$ denotes concatenation along the feature dimension, and $\sin(\cdot)$ and $\cos(\cdot)$ are applied element-wise. L is the number of frequency bands in the positional encoding. Next, we feed \mathbf{r}_{in} into a lightweight MLP with ReLU activation to produce low-rank positional representations that parameterize an implicit neural field for positional bias. Specifically, we first compute a shared hidden representation $\mathbf{h} \in \mathbb{R}^{N \times d_h}$ as:

$$\mathbf{h} = \text{ReLU}(\mathbf{r}_{\text{in}} \mathbf{W}_h + \mathbf{b}_h), \quad (2)$$

where $\mathbf{W}_h \in \mathbb{R}^{(2+4L) \times d_h}$ and $\mathbf{b}_h \in \mathbb{R}^{d_h}$. We then linearly project \mathbf{h} into a low-rank space of dimension R , as follows:

$$\mathbf{Q}_p = \mathbf{h} \mathbf{W}_{p,q}, \quad \mathbf{K}_p = \mathbf{h} \mathbf{W}_{p,k}, \quad (3)$$

where $\mathbf{W}_{p,q}, \mathbf{W}_{p,k} \in \mathbb{R}^{d_h \times R}$. In practice, we share the hidden representation \mathbf{h} across all attention heads, and obtain head-wise \mathbf{Q}_p and \mathbf{K}_p via separate linear projections from the shared \mathbf{h} . Next, unlike vanilla self-attention that directly forms $\mathbf{Q} = X \mathbf{W}_q$ and $\mathbf{K} = X \mathbf{W}_k$, we explicitly separate content and positional components. Given token features X , we define the content projections

$$\mathbf{Q}_c = X \mathbf{W}_q, \quad \mathbf{K}_c = X \mathbf{W}_k, \quad (4)$$

while keeping the value projection identical to standard attention ($\mathbf{V} = X \mathbf{W}_v$). Then, we merge content and positional components by channel-wise concatenation. Specifically, we scale \mathbf{Q}_c and \mathbf{Q}_p by their respective dimensions and construct

$$\mathbf{Q} = \left[\mathbf{Q}_c / \sqrt{D}, \mathbf{Q}_p / \sqrt{R} \right], \quad \mathbf{K} = \left[\mathbf{K}_c, \mathbf{K}_p \right]. \quad (5)$$

The resulting scaled similarity matrix is obtained as a single dot-product in the augmented channel space:

$$\mathbf{S} = \mathbf{Q} \mathbf{K}^\top = \underbrace{(\mathbf{Q}_c \mathbf{K}_c^\top) / \sqrt{D}}_{\text{content term}} + \underbrace{(\mathbf{Q}_p \mathbf{K}_p^\top) / \sqrt{R}}_{\text{bias term}}, \quad (6)$$

which shows that the spatial prior is injected as an additive bias term in the logits while remaining decoupled from the pixel content term in logit space.

The subsequent steps operate identically to standard self-attention (e.g., $\mathbf{O} = \text{SoftMax}(\mathbf{S})\mathbf{V}$).

In summary, RIB is fully compatible with existing FlashAttention implementations, similar to RoPE, because it injects positional priors by augmenting \mathbf{Q} and \mathbf{K} and computing the logits via a single dot-product, without requiring any extra $N \times N$ bias matrix materialization or table indexing. Moreover, unlike RPB, whose number of bias parameters grows with the window size (e.g., $(2M - 1)^2 \approx O(M^2)$), RIB parameterizes the positional bias using a lightweight MLP, making the number of bias parameters independent of the window size (e.g., $O(d_h(L + R))$). Finally, since \mathbf{Q}_p and \mathbf{K}_p depend only on the window geometry (normalized coordinates) and not on the input pixel contents, they can be precomputed and cached, further reducing inference-time overhead.

3.2 Convolutional Local Attention

Due to the low-rank nature of the RIB, it may be less effective for certain highly localized, rapidly varying positional patterns. We therefore further enhance RIB with a CLA that is designed to strengthen short-range interactions and help capture fine details. Technically, given the token features X , we define a pair of reshaping operators \mathcal{F} and \mathcal{F}^{-1} that convert between token features and 2D feature maps:

$$\mathcal{F} : \mathbb{R}^{B \times H \times W \times D} \rightarrow \mathbb{R}^{B \times N \times D}, \quad \mathcal{F}^{-1} : \mathbb{R}^{B \times N \times D} \rightarrow \mathbb{R}^{B \times H \times W \times D}. \quad (7)$$

We first restore X to an image-shaped 2D feature map \tilde{X} to enable convolution:

$$\tilde{X} = \mathcal{F}^{-1}(X) \in \mathbb{R}^{B \times H \times W \times D}. \quad (8)$$

CLA then generates a locally informed gating map via a lightweight convolutional path consisting of a 3×3 depth-wise convolution, a 1×1 point-wise convolution, and a sigmoid activation:

$$\tilde{\mathbf{G}} = \sigma\left(\text{PWConv}\left(\text{DWConv}_{3 \times 3}(\tilde{X})\right)\right) \in \mathbb{R}^{B \times H \times W \times D}. \quad (9)$$

The resulting gating map is then converted back to token form to align with the attention output:

$$\mathbf{G} = \mathcal{F}(\tilde{\mathbf{G}}) \in \mathbb{R}^{B \times N \times D}. \quad (10)$$

We then modulate the self-attention output $\mathbf{O} \in \mathbb{R}^{B \times N \times D}$ by the gating map via element-wise multiplication:

$$\mathbf{O}' = \mathbf{O} \odot \mathbf{G}, \quad (11)$$

where $\text{DWConv}_{3 \times 3}$ and PWConv denote depth-wise and point-wise convolutions, $\sigma(\cdot)$ is the sigmoid activation, and \odot denotes element-wise multiplication.

In summary, CLA selectively emphasizes spatially consistent high-frequency responses, aiding self-attention with RIB to focus on larger and broader patterns. Moreover, compared to the output projection of standard self-attention ($Y = \mathbf{O}\mathbf{W}_o$), where \mathbf{W}_o denotes output projection weight matrix, CLA provides additional non-linearity before output projection ($Y = (\mathbf{O} \odot \mathbf{G})\mathbf{W}_o$), further enhancing the representational capability of Transformers [46].

3.3 Cyclic Window Strategy

Thanks to the memory efficiency enabled by FlashAttention and our proposed RIB, we can employ substantially larger attention windows without incurring prohibitive memory overhead. Nevertheless, prior works have highlighted that combining relatively small windows is beneficial for multi-scale feature extraction [69, 70]. Motivated by this, we propose a simple cyclic window strategy that balances local detail modeling and long-range interaction by periodically varying the window size across consecutive self-attentions. Specifically, we cycle the window size from small to large and repeat the cycle twice within a block (e.g. {16, 32, 64, 16, 32, 64}). This periodic expansion provides repeated global mixing while preserving local refinements.

4 Experiments

We evaluate our method in terms of (i) training and inference efficiency, (ii) quantitative SR performance, (iii) ablations, and (iv) qualitative analyses, including local attribution maps (LAM), positional bias visualization, and visual results. We introduce our SR Transformer using a 64×64 attention window, termed as **SST** (12M), and a parameter-scaled-up variant **SST-L** (20M). Models using a larger attention window (up to 96×96) are denoted with "+".

Since SR methods are typically trained on 64×64 cropped patches, naively applying a 96×96 window would introduce substantial padding to match the feature size to the window size, which can destabilize optimization. Therefore, we train the "+" variants with 96×96 training patches, and this setting is marked with "†". Despite the larger training patches, our method remains faster and more memory-efficient than prior methods trained with 64×64 patches, thanks to FlashAttention enabled by RIB, as shown in Section 4.1. Additional implementation details and results on lightweight networks are provided in the supplementary material.

4.1 Comparisons of Training and Inference Costs

We first compare the training and inference costs of our method against representative SR baselines to highlight the efficiency gains enabled by FlashAttention. As reported in Table 1, SST-L achieves the lowest training time and memory footprint, as well as lower inference latency and memory, despite leveraging a much larger attention window. This demonstrates that FlashAttention can provide substantial end-to-end benefits. Next, we compare SST-L+ with ATD under the same 96×96 training patch setting. SST-L+ is $1.92\times$ faster in training while using $1.9\times$ less training memory. This result indicates that naively increasing the training patch size without an appropriate hardware-efficient kernel can introduce significant overhead, and it reinforces the importance of FlashAttention for scaling SR Transformers. We also compare SST-L+ with PFT. Although SST-L+ requires $5.7\times$ more FLOPs, it uses about $10\times$ less inference memory and

Table 1: Comparison of training and inference costs across SR methods. Training costs are measured using the batch size of 10, which is the largest batch size that does not cause an OOM in all cases. Inference costs are measured while reconstructing a 1280×720 image at scale $\times 2$. All statistics are measured using an H200 GPU at FP32 precision. The best result is bolded. We leverage FlashAttention3 [49] for the hardware-efficient acceleration kernel. For more comparisons across various GPUs and FlashAttention implementations, please refer to the supplementary materials.

Method	Training			Inference			
	patch size	sec/step	memory	#FLOPs	#params	latency	memory
HAT [5]	64×64	0.432	32.4GB	5.81T	20.6M	709.9ms	9070MB
ATD [68]	96×96	1.291	132.5GB	6.07T	20.1M	1266.8ms	6239MB
PFT [36]	64×64	1.410	85.4GB	5.03T	19.6M	1920.8ms	28869MB
MambaIR [22]	64×64	0.791	50.0GB	5.87T	20.4M	1043.8ms	7704MB
MambaIRV2-L [21]	64×64	1.210	89.8GB	9.42T	34.1M	2308.8ms	5816MB
SST-L	64×64	0.370	31.4GB	18.8T	20.3M	608.4ms	2823MB
SST-L+	96×96	0.672	67.7GB	28.7T	20.3M	644.9ms	2989MB

achieves roughly $3 \times$ lower latency. We argue that this discrepancy stems from the fact that FLOPs reductions do not necessarily reflect practical efficiency gains [4, 37, 64]. Although PFT reduces FLOPs through top- k sparsification, it still needs to materialize $N \times N$ and $N \times K$ matrices for each window (including shifted-window attention), such as the previous layer’s similarity matrix \mathbf{S} and sparsification index matrix \mathbf{I} . As a result, PFT is primarily bottlenecked by memory traffic rather than computation, which leads to higher latency and increased memory consumption. Finally, even when processing high-resolution feature maps (e.g., 640×360 features for 1280×720 reconstruction at $\times 2$), SST-L+ remains more efficient in inference than Mamba-based (linear-operator) SR methods, underscoring the practicality and promise of FlashAttention-equipped Transformers.

4.2 Quantitative Results

Next, we conduct a quantitative comparison to demonstrate the strong performance of our method. For this comparison, we crop the boundary of the I_{SR} by the upscaling factor, convert the result to the YCbCr color space, and then compute PSNR and SSIM on the Y channel, following standard convention. *Please note that we compare against methods for which both the official code and pretrained weights are publicly available.*

Results on DF2K Datasets We compare our proposed networks (SST, SST+, SST-L, and SST-L+), trained on the DF2K dataset [1, 57], with representative SR methods employing different core operators, including Transformers [5, 8, 30, 32, 36, 67, 68], a graph neural network (GNN) [56], and Mamba [21, 22]. All evaluations are conducted on commonly used benchmark datasets, including Set5 [2], Set14 [66], BSD100 [38], Urban100 [25], and Manga109 [39]. As shown in Table 2,

Table 2: Quantitative comparison (PSNR/SSIM) on benchmark datasets trained on DF2K datasets [1, 57]. [†] denotes the method is trained using 96×96 patches. The best result is bolded.

Method	Venue	scale #params	Set5	Set14	BSD100	Urban100	Manga109	
			PSNR/SSIM	PSNR/SSIM	PSNR/SSIM	PSNR/SSIM	PSNR/SSIM	
SwinIR [32]	ICCVW'21	11.8	38.42/0.9623	34.46/0.9250	32.53/0.9041	33.81/0.9427	39.92/0.9797	
ESC [†] [30]	ICCV'25	12.5	38.59/0.9630	34.70/0.9259	32.61/0.9052	34.49/0.9466	40.38/0.9809	
CAT-A [8]	NeurIPS'22	16.5	38.51/0.9626	34.78/0.9265	32.59/0.9047	34.26/0.9440	40.10/0.9805	
ART [67]	ICLR'23	16.4	38.56/0.9629	34.59/0.9267	32.58/0.9048	34.30/0.9452	40.24/0.9808	
HAT [5]	CVPR'23	20.6	38.63/0.9630	34.86/0.9274	32.62/0.9053	34.45/0.9466	40.26/0.9809	
ATD [†] [68]	CVPR'24	20.1	38.61/0.9629	34.95/0.9276	32.65/0.9056	34.70/0.9476	40.37/0.9810	
PFT [36]	CVPR'25	19.6	38.68/0.9635	35.00/0.9280	32.67/0.9058	34.90/0.9490	40.49/0.9815	
IPG [56]	CVPR'24	×2	20.4	38.61/0.9632	34.73/0.9270	32.60/0.9052	34.48/0.9464	40.24/0.9810
MambaIR [22]	ECCV'24	20.4	38.57/0.9627	34.67/0.9261	32.58/0.9048	34.15/0.9446	40.28/0.9806	
MambaIRV2-S [21]	CVPR'25	9.6	38.53/0.9627	34.62/0.9256	32.59/0.9048	34.24/0.9454	40.27/0.9808	
MambaIRV2-B [21]	CVPR'25	22.9	38.65/0.9631	34.89/0.9275	32.62/0.9053	34.49/0.9468	40.42/0.9810	
MambaIRV2-L [21]	CVPR'25	34.1	38.65/0.9632	34.93/0.9276	32.62/0.9053	34.60/0.9475	40.55/0.9807	
SST	-	11.7	38.63/0.9629	34.72/0.9258	32.55/0.9042	34.61/0.9474	40.31/0.9808	
SST+ [†]	-	11.7	38.63/0.9631	34.89/0.9273	32.62/0.9053	34.88/0.9488	40.44/0.9812	
SST-L	-	20.3	38.65/0.9631	34.86/0.9270	32.60/0.9050	34.78/0.9485	40.44/0.9812	
SST-L+ [†]	-	20.3	38.64/0.9630	34.94/0.9273	32.61/0.9050	35.01/0.9497	40.56/0.9815	
SwinIR [32]	ICCVW'21	11.9	34.97/0.9318	30.93/0.8534	29.46/0.8145	29.75/0.8826	35.12/0.9537	
ESC [†] [30]	ICCV'25	12.5	35.14/0.9330	31.10/0.8552	29.53/0.8167	30.23/0.8895	35.60/0.9555	
CAT-A [8]	NeurIPS'22	16.6	35.06/0.9326	31.04/0.8538	29.52/0.8160	30.12/0.8862	35.38/0.9546	
ART [67]	ICLR'23	16.6	35.07/0.9325	31.02/0.8541	29.51/0.8159	30.10/0.8871	35.39/0.9548	
HAT [5]	CVPR'23	20.8	35.07/0.9329	31.08/0.8555	29.54/0.8167	30.23/0.8896	35.53/0.9552	
ATD [†] [68]	CVPR'24	20.3	35.11/0.9330	31.13/0.8556	29.57/0.8176	30.46/0.8917	35.63/0.9558	
PFT [36]	CVPR'25	19.8	35.15/0.9333	31.16/0.8561	29.58/0.8178	30.56/0.8931	35.67/0.9560	
IPG [56]	CVPR'24	×3	18.3	35.10/0.9332	31.10/0.8554	29.53/0.8168	30.36/0.8901	35.53/0.9554
MambaIR [22]	ECCV'24	20.4	35.08/0.9323	30.99/0.8536	29.51/0.8157	29.93/0.8841	35.43/0.9546	
MambaIRV2-S [21]	CVPR'25	9.8	35.09/0.9326	31.07/0.8547	29.51/0.8157	30.08/0.8871	35.44/0.9549	
MambaIRV2-B [21]	CVPR'25	23.1	35.18/0.9334	31.12/0.8557	29.55/0.8169	30.28/0.8905	35.61/0.9556	
MambaIRV2-L [21]	CVPR'25	34.2	35.16/0.9334	31.18/0.8564	29.57/0.8175	30.34/0.8912	35.72/0.9561	
SST	-	11.9	35.10/0.9323	31.00/0.8533	29.46/0.8149	30.35/0.8909	35.56/0.9554	
SST+ [†]	-	11.9	35.19/0.9335	31.08/0.8553	29.54/0.8170	30.59/0.8941	35.66/0.9560	
SST-L	-	20.7	35.13/0.9328	31.02/0.8544	29.47/0.8152	30.52/0.8934	35.61/0.9557	
SST-L+ [†]	-	20.7	35.25/0.9337	31.16/0.8550	29.56/0.8174	30.75/0.8962	35.83/0.9568	
SwinIR [32]	ICCVW'21	11.9	32.92/0.9044	29.09/0.7950	27.92/0.7489	27.45/0.8254	32.03/0.9260	
ESC [†] [30]	ICCV'25	12.5	33.00/0.9054	29.21/0.7968	27.95/0.7504	27.89/0.8351	32.54/0.9295	
CAT-A [8]	NeurIPS'22	16.6	33.08/0.9052	29.18/0.7960	27.99/0.7510	27.89/0.8339	32.39/0.9285	
ART [67]	ICLR'23	16.6	33.04/0.9051	29.16/0.7958	27.97/0.7510	27.77/0.8321	32.31/0.9283	
HAT [5]	CVPR'23	20.8	33.04/0.9056	29.23/0.7973	28.00/0.7517	27.97/0.8368	32.48/0.9292	
ATD [†] [68]	CVPR'24	20.3	33.10/0.9058	29.24/0.7974	28.01/0.7526	28.17/0.8404	32.62/0.9306	
PFT [36]	CVPR'25	19.8	33.15/ 0.9065	29.29/0.7978	28.02/0.7527	28.20/0.8412	32.63/0.9306	
IPG [56]	CVPR'24	×4	17.0	33.15/0.9062	29.24/0.7973	27.99/0.7519	28.13/0.8392	32.53/0.9300
MambaIR [22]	ECCV'24	20.4	33.03/0.9046	29.20/0.7961	27.98/0.7503	27.68/0.8287	32.32/0.9272	
MambaIRV2-S [21]	CVPR'25	9.8	32.99/0.9037	29.23/0.7965	27.97/0.7502	27.73/0.8307	32.33/0.9276	
MambaIRV2-B [21]	CVPR'25	23.1	33.14/0.9057	29.23/0.7975	28.00/0.7511	27.89/0.8344	32.57/0.9295	
MambaIRV2-L [21]	CVPR'25	34.2	33.19/0.9062	29.29/0.7982	28.01/0.7521	28.07/0.8383	32.66/0.9304	
SST	-	12.1	33.15/0.9059	29.21/0.7966	27.96/0.7505	28.08/0.8389	32.52/0.9295	
SST+ [†]	-	12.1	33.00/0.9054	29.21/0.7971	27.96/0.7511	28.23/0.8427	32.66/0.9308	
SST-L	-	21.3	33.08/0.9056	29.25/0.7980	27.96/0.7511	28.23/0.8432	32.64/0.9305	
SST-L+ [†]	-	21.3	33.12/0.9057	29.23/0.7973	27.98/0.7512	28.39/0.8466	32.85/0.9322	

SST achieves superior performance on Urban100×2, outperforming HAT (20M parameters) by 0.16 dB while using only 12M parameters, demonstrating the effectiveness of our 64×64 large-window attention. Furthermore, when trained with 96×96 patches, SST+ (12M parameters) surpasses ATD (20M parameters) trained under the same setting by 0.18 dB on Urban100×2, indicating that SST+ more effectively exploits the benefits of 96×96 large-window attention. The parameter-scaled variants up to 20M (SST-L and SST-L+) consistently

Table 3: Quantitative comparison (PSNR/SSIM) on benchmark datasets trained on DFLIP datasets [1, 31, 42, 57]. [†] denotes the method is trained using 96×96 patches. The best result is bolded.

Method	scale #params	Set5	Set14	BSD100	Urban100	Manga109	DIV2K-val	LSDIR-val	
		PSNR/SSIM	PSNR/SSIM	PSNR/SSIM	PSNR/SSIM	PSNR/SSIM	PSNR/SSIM	PSNR/SSIM	
PFT [36]	19.6	38.67/0.9633	35.11/0.9282	32.71/0.9062	35.24/0.9508	40.64/0.9817	37.17/0.9526	32.92/0.9321	
MambaRV2-L [21]	$\times 2$	34.2	38.77/0.9636	35.20/0.9287	32.74/0.9065	35.20/0.9508	40.82/0.9820	37.16/0.9524	32.93/0.9321
SST-L	20.3	38.70/0.9635	35.06/0.9274	32.69/0.9058	35.35/0.9515	40.64/0.9817	37.21/0.9528	32.97/0.9325	
SST-L+ [†]	20.3	38.78/0.9637	35.28/0.9288	32.73/0.9064	35.63/0.9530	40.86/0.9821	37.32/0.9535	33.12/0.9338	
PFT [36]	19.8	35.12/0.9335	31.45/0.8572	29.60/0.8188	31.08/0.8996	35.81/0.9567	33.41/0.9020	29.16/0.8578	
MambaRV2-L [21]	$\times 3$	34.2	35.23/0.9341	31.56/0.8586	29.66/0.8195	31.13/0.9000	35.98/0.9574	33.43/0.9020	29.23/0.8586
SST-L	20.7	35.24/0.9339	31.47/0.8567	29.57/0.8177	31.22/0.9010	35.90/0.9570	33.45/0.9026	29.21/0.8587	
SST-L+ [†]	20.7	35.33/0.9345	31.54/0.8576	29.64/0.8193	31.53/0.9046	36.12/0.9580	33.55/0.9037	29.33/0.8609	
PFT [36]	19.8	33.17/0.9071	29.50/0.8005	28.03/0.7537	28.71/0.8515	32.84/0.9323	31.38/0.8573	27.22/0.7950	
MambaRV2-L [21]	$\times 4$	34.2	33.20/0.9073	29.57/ 0.8018	28.11/0.7556	28.75/0.8526	32.99/0.9334	31.40/0.8576	27.29/0.7967
SST-L	21.3	33.25/0.9080	29.58/0.8016	28.07/0.7541	28.90/0.8549	33.00/0.9334	31.44/0.8584	27.31/0.7972	
SST-L+ [†]	21.3	33.10/0.9067	29.58/0.8016	28.06/0.7541	29.06/0.8583	33.18/0.9345	31.50/0.8594	27.37/0.7991	

achieve strong performance on Urban100 and Manga109 across all upscaling factors, showing that our methods are competitive with prior SOTA approaches. Notably, these improvements come with substantially reduced training and inference costs, as demonstrated in Section 4.1.

Results on DFLIP Datasets Our method exhibits remarkable gains in the mid-size regime (11M parameters), even surpassing prior 20M parameter models. However, when scaling to the 20M parameter regime, our results become largely comparable to existing approaches. We hypothesize that this behavior stems from data limitations in standard SR training: given the strong representational capacity of our network, the commonly used training data may be insufficient, leading to overfitting. To examine this hypothesis, we train our models as well as representative SOTA baselines (PFT and MambaRV2-L) on the DFLIP training setting, which augments the widely used DF2K dataset with additional large-scale datasets, such as LSDIR [31] and DiverSeg-IP [42]. We adopt the same training setup as in the DF2K experiments to ensure a fair comparison. In addition, to broaden the evaluation scope, we report results on DIV2K-val [1] and LSDIR-val [31], which have been less commonly included in prior comparisons. As shown in Table 3, when trained on DF2K only, SST-L underperforms PFT by 0.12 dB on Urban100 $\times 2$, whereas when trained on DFLIP, it surpasses PFT by 0.11 dB, highlighting the strong data-scaling capability of our approach. Moreover, SST-L+ consistently delivers substantial improvements over prior SOTA methods across all upscaling factors on Urban100, Manga109, DIV2K-val, and LSDIR-val, demonstrating that our scaling design choices, including window size, training patch size, and data size, are highly effective.

4.3 Ablation Studies

Next, we conduct ablation studies to verify that our proposal is effective and that the implementation is appropriate. As shown in Table 4, our proposed RIB achieves the second-best performance following FlexAttention with RPB [15, 30],

Table 4: Training/inference costs and performance of attention/bias variants on SST+. Training and inference costs are measured as detailed in Table 1.

Attention	Bias	Training		Inference			Urban100	Manga109
		sec/step	memory	#params	latency	memory	PSNR/SSIM	PSNR/SSIM
Naive	RPB [35]	-	-	13.6M	11705.3ms	126181MB	- / -	- / -
FlexAttention [15,30]	RPB [35]	5.048	47.2GB	13.6M	2414.0ms	2487MB	34.91/0.9489	40.42/0.9812
FlashAttention3 [49]	CPE [10]	0.625	46.5GB	11.3M	537.3ms	2354MB	Not Converged	
FlashAttention3 [49]	FlashBias [61]	0.473	47.3GB	46.7M	455.7ms	2825MB	Not Converged	
FlashAttention3 [49]	RoPE-ViT [23]	0.489	47.9GB	11.3M	432.7ms	2915MB	34.71/0.9479	40.40/0.9811
FlashAttention3 [49]	RIB (Ours)	0.479	47.1GB	11.7M	455.7ms	2825MB	34.88/0.9488	40.44/0.9812

Table 5: Ablation analysis of various components in the proposed SST on Urban100 and Manga109 (PSNR/SSIM).

(a) Gating Type			(b) Window Strategy			(c) Fourier Embedding		
Gating Type	Urban100	Manga109	Window Strategy	Urban100	Manga109	Fourier Emb.	Urban100	Manga109
Without G	Not Converged		{4, 8, 16, 32, 64, 64}	34.56/0.9470	40.22/0.9807	$L=5$	34.20/0.9447	39.96/0.9797
Only PWConv [46]	34.55/0.9473	40.24/0.9807	{64, 64, 32, 16, 8, 4}	34.51/0.9468	40.17/0.9804	$L=15$	34.48/0.9468	40.17/0.9805
CLA	34.61/0.9474	40.31/0.9808	{64, 64, 64, 64, 64, 64}	34.54/0.9468	40.19/0.9806	SIREN [52]	Not Converged	
			{16, 32, 64, 16, 32, 64}	34.61/0.9474	40.31/0.9808	$L=10$	34.61/0.9474	40.31/0.9808

while offering substantially improved efficiency (e.g., $10.5\times$ faster training and $5\times$ faster inference). Moreover, our RIB demonstrates stable results compared with methods that cannot directly incorporate a spatial prior into self-attention, such as conditional positional encoding (CPE [10]) or FlashBias [61] trained from scratch. Finally, RIB demonstrates superior performance over the RoPE-based method [23], suggesting that preserving pixel integrity is effective.

In addition, Table 5 presents further ablations on our proposed CLA, the cyclic window strategy, and the number of frequency bands used in RIB (L). First, incorporating CLA yields higher performance than configurations without any **G**, which tend to diverge, as well as variants using only PWConv, demonstrating that CLA contributes meaningfully to the performance gains. Next, the cyclic window strategy achieves better results than schedules that monotonically increase or decrease the window size, and even outperforms using a fixed 64×64 window throughout, suggesting that it strikes an effective balance between multi-scale feature extraction and long-range modeling. Finally, setting $L=10$ delivers the best performance compared to other numbers or using SIREN [52] activations. This observation is consistent with findings reported in previous research [41, 54] on the novel view synthesis task.

4.4 Positional Bias Visualization

To verify whether RIB effectively captures positional bias, we conduct a visualization analysis. As shown in Figure 4, the bias generated by RIB assigns high correlation locally to nearby pixels and also induces strong correlations along the vertical (up and down) direction. This indicates that RIB effectively provides a spatial prior to the self-attention.

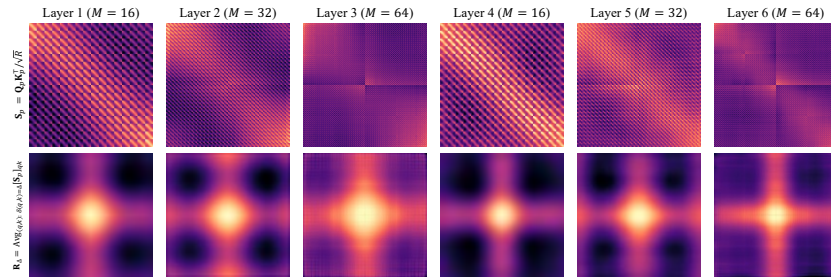


Fig. 4: Visualized positional score matrix (\mathbf{S}_P) and relative positional bias table (\mathbf{R}_Δ) calculated from the second block of SST. We average the biases that correspond to the same 2D distance, since positional bias predicted by our RIB does not guarantee equivalence across the same relative offsets.

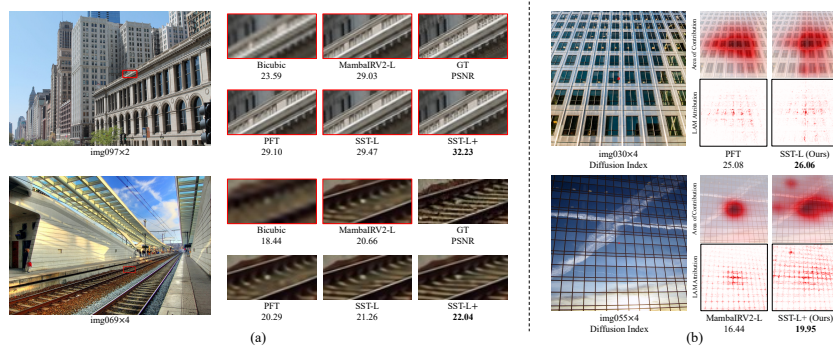


Fig. 5: Comparisons of (a) visual results and (b) local attribution maps (LAM) [20]. Since padding/cropping for windowing inside the networks hinders accurate comparison, we separately compare SST-L (512×512 patch) and SST-L+ (768×768 patch).

4.5 Local Attribution Map and Visual Results

Finally, through a visual comparison, we verify that our networks restore visually superior results and leverage a wider receptive field. As illustrated in Figure 5, our networks restore fine details most faithfully, achieving the highest PSNR while leveraging the broadest receptive field around edges.

5 Conclusion

In this paper, we propose a FlashAttention-compatible bias termed RIB for SR Transformers that preserves the integrity of pixel representations, along with CLA and a cyclic window strategy to further strengthen long-range interactions. Leveraging these components, we simply scale up both the self-attention window size and two factors that have been relatively underexplored in prior work—training patch size and dataset size. Consequently, we substantially reduce both training and inference costs while achieving 29.06 dB PSNR on Urban100 \times 4, highlighting the promise of this underexplored direction for SR tasks.

References

1. Agustsson, E., Timofte, R.: Ntire 2017 challenge on single image super-resolution: Dataset and study. In: CVPRW (July 2017)
2. Bevilacqua, M., Roumy, A., Guillemot, C., Alberi-Morel, M.L.: Low-complexity single-image super-resolution based on nonnegative neighbor embedding (2012)
3. Caron, M., Touvron, H., Misra, I., Jégou, H., Mairal, J., Bojanowski, P., Joulin, A.: Emerging properties in self-supervised vision transformers. In: ICCV. pp. 9650–9660 (2021)
4. Chen, J., Kao, S.h., He, H., Zhuo, W., Wen, S., Lee, C.H., Chan, S.H.G.: Run, don’t walk: chasing higher flops for faster neural networks. In: CVPR. pp. 12021–12031 (2023)
5. Chen, X., Wang, X., Zhou, J., Qiao, Y., Dong, C.: Activating more pixels in image super-resolution transformer. In: CVPR. pp. 22367–22377 (2023)
6. Chen, Z., Zhang, Y., Gu, J., Kong, L., Yang, X.: Recursive generalization transformer for image super-resolution. In: ICLR (2024)
7. Chen, Z., Zhang, Y., Gu, J., Kong, L., Yang, X., Yu, F.: Dual aggregation transformer for image super-resolution. In: ICCV. pp. 12312–12321 (2023)
8. Chen, Z., Zhang, Y., Gu, J., Zhang, Y., Kong, L., Yuan, X.: Cross aggregation transformer for image restoration. In: NeurIPS (2022)
9. Choi, H., Lee, J., Yang, J.: N-gram in swin transformers for efficient lightweight image super-resolution. In: CVPR. pp. 2071–2081 (2023)
10. Chu, X., Tian, Z., Zhang, B., Wang, X., Shen, C.: Conditional positional encodings for vision transformers. In: ICLR (2023), <https://openreview.net/forum?id=3KWnuT-R1bh>
11. Dao, T.: Flashattention-2: Faster attention with better parallelism and work partitioning. arXiv (2023)
12. Dao, T., Fu, D., Ermon, S., Rudra, A., Ré, C.: Flashattention: Fast and memory-efficient exact attention with io-awareness. NeurIPS **35**, 16344–16359 (2022)
13. Dong, C., Loy, C.C., He, K., Tang, X.: Image super-resolution using deep convolutional networks. IEEE TPAMI **38**(2), 295–307 (2015)
14. Dong, C., Loy, C.C., Tang, X.: Accelerating the super-resolution convolutional neural network. In: ECCV. pp. 391–407. Springer (2016)
15. Dong, J., Feng, B., Guessous, D., Liang, Y., He, H.: Flex attention: A programming model for generating optimized attention kernels. arXiv (2024)
16. Dosovitskiy, A., Beyer, L., Kolesnikov, A., Weissenborn, D., Zhai, X., Unterthiner, T., Dehghani, M., Minderer, M., Heigold, G., Gelly, S., et al.: An image is worth 16x16 words: Transformers for image recognition at scale. ICLR (2020)
17. Du, Z., Liu, J., Tang, J., Wu, G.: Anchor-based plain net for mobile image super-resolution. In: CVPRW. pp. 2494–2502 (2021)
18. Grattafiori, A., Dubey, A., Jauhri, A., Pandey, A., Kadian, A., Al-Dahle, A., Letman, A., Mathur, A., Schelten, A., Vaughan, A., et al.: The llama 3 herd of models. arXiv (2024)
19. Gu, A., Dao, T.: Mamba: Linear-time sequence modeling with selective state spaces. arXiv preprint (2023)
20. Gu, J., Dong, C.: Interpreting super-resolution networks with local attribution maps. In: CVPR. pp. 9199–9208 (2021)
21. Guo, H., Guo, Y., Zha, Y., Zhang, Y., Li, W., Dai, T., Xia, S.T., Li, Y.: Mambairv2: Attentive state space restoration. CVPR (2025)

22. Guo, H., Li, J., Dai, T., Ouyang, Z., Ren, X., Xia, S.T.: Mambair: A simple baseline for image restoration with state-space model. In: ECCV (2024)
23. Heo, B., Park, S., Han, D., Yun, S.: Rotary position embedding for vision transformer. In: ECCV. pp. 289–305. Springer (2024)
24. Hu, Q., Tang, Y., Zhang, X.: Large kernel modulation network for efficient image super-resolution. arXiv (2025)
25. Huang, J.B., Singh, A., Ahuja, N.: Single image super-resolution from transformed self-exemplars. In: CVPR. pp. 5197–5206 (2015)
26. Kim, J., Lee, J.K., Lee, K.M.: Accurate image super-resolution using very deep convolutional networks. In: CVPR. pp. 1646–1654 (2016)
27. Kirillov, A., Mintun, E., Ravi, N., Mao, H., Rolland, C., Gustafson, L., Xiao, T., Whitehead, S., Berg, A.C., Lo, W.Y., et al.: Segment anything. In: ICCV. pp. 4015–4026 (2023)
28. Lee, D., Yun, S., Ro, Y.: Implicit grid convolution for multi-scale image super-resolution. arXiv (2024)
29. Lee, D., Yun, S., Ro, Y.: Partial large kernel cnns for efficient super-resolution. arXiv (2024)
30. Lee, D., Yun, S., Ro, Y.: Emulating self-attention with convolution for efficient image super-resolution. In: ICCV. pp. 24467–24477 (October 2025)
31. Li, Y., Zhang, K., Liang, J., Cao, J., Liu, C., Gong, R., Zhang, Y., Tang, H., Liu, Y., Demandolx, D., et al.: Lsdir: A large scale dataset for image restoration. In: CVPRW. pp. 1775–1787 (2023)
32. Liang, J., Cao, J., Sun, G., Zhang, K., Van Gool, L., Timofte, R.: Swinir: Image restoration using swin transformer. In: ICCVW. pp. 1833–1844 (2021)
33. Lim, B., Son, S., Kim, H., Nah, S., Mu Lee, K.: Enhanced deep residual networks for single image super-resolution. In: CVPRW. pp. 136–144 (2017)
34. Lin, Z., Garg, P., Banerjee, A., Magid, S.A., Sun, D., Zhang, Y., Van Gool, L., Wei, D., Pfister, H.: Revisiting rcnn: Improved training for image super-resolution. arXiv (2022)
35. Liu, Z., Lin, Y., Cao, Y., Hu, H., Wei, Y., Zhang, Z., Lin, S., Guo, B.: Swin transformer: Hierarchical vision transformer using shifted windows. In: ICCV. pp. 10012–10022 (2021)
36. Long, W., Zhou, X., Zhang, L., Gu, S.: Progressive focused transformer for single image super-resolution. In: CVPR. pp. 2279–2288 (2025)
37. Ma, N., Zhang, X., Zheng, H.T., Sun, J.: Shufflenet v2: Practical guidelines for efficient cnn architecture design. In: ECCV. pp. 116–131 (2018)
38. Martin, D., Fowlkes, C., Tal, D., Malik, J.: A database of human segmented natural images and its application to evaluating segmentation algorithms and measuring ecological statistics. In: ICCV. vol. 2, pp. 416–423. IEEE (2001)
39. Matsui, Y., Ito, K., Aramaki, Y., Fujimoto, A., Ogawa, T., Yamasaki, T., Aizawa, K.: Sketch-based manga retrieval using manga109 dataset. *Multimedia tools and applications* **76**, 21811–21838 (2017)
40. Meng, C., Long, W., Gu, S.: From local windows to adaptive candidates via individualized exploratory: Rethinking attention for image super-resolution. arXiv (2026)
41. Mildenhall, B., Srinivasan, P.P., Tancik, M., Barron, J.T., Ramamoorthi, R., Ng, R.: Nerf: Representing scenes as neural radiance fields for view synthesis. In: ECCV (2020)
42. Ohtani, G., Tadokoro, R., Yamada, R., Asano, Y.M., Laina, I., Rupperecht, C., Inoue, N., Yokota, R., Kataoka, H., Aoki, Y.: Rethinking image super-resolution from training data perspectives. In: ECCV. pp. 19–36. Springer (2024)

43. Oquab, M., Darcet, T., Moutakanni, T., Vo, H., Szafraniec, M., Khalidov, V., Fernandez, P., Haziza, D., Massa, F., El-Nouby, A., et al.: Dinov2: Learning robust visual features without supervision. TMLR (2023)
44. Park, K., Cho, N.I.: Partial filter-sharing: Improved parameter-sharing method for single image super-resolution networks. In: WACV. pp. 2653–2663. IEEE (2025)
45. Park, K., Soh, J.W., Cho, N.I.: Efficient attention-sharing information distillation transformer for lightweight single image super-resolution. In: AAAI (2025)
46. Qiu, Z., Wang, Z., Zheng, B., Huang, Z., Wen, K., Yang, S., Men, R., Yu, L., Huang, F., Huang, S., et al.: Gated attention for large language models: Non-linearity, sparsity, and attention-sink-free. In: NeurIPS (2025)
47. Raffel, C., Shazeer, N., Roberts, A., Lee, K., Narang, S., Matena, M., Zhou, Y., Li, W., Liu, P.J.: Exploring the limits of transfer learning with a unified text-to-text transformer. *Journal of machine learning research* **21**(140), 1–67 (2020)
48. Ray, A., Kumar, G., Kolekar, M.H.: Cfat: Unleashing triangular windows for image super-resolution. In: CVPR. pp. 26120–26129 (2024)
49. Shah, J., Bikshandi, G., Zhang, Y., Thakkar, V., Ramani, P., Dao, T.: Flashattention-3: Fast and accurate attention with asynchrony and low-precision. *NeurIPS* **37**, 68658–68685 (2024)
50. Shi, W., Caballero, J., Huszár, F., Totz, J., Aitken, A.P., Bishop, R., Rueckert, D., Wang, Z.: Real-time single image and video super-resolution using an efficient sub-pixel convolutional neural network. In: CVPR. pp. 1874–1883 (2016)
51. Simonyan, K., Zisserman, A.: Very deep convolutional networks for large-scale image recognition. *arXiv* (2014)
52. Sitzmann, V., Martel, J., Bergman, A., Lindell, D., Wetzstein, G.: Implicit neural representations with periodic activation functions. *NeurIPS* **33**, 7462–7473 (2020)
53. Su, J., Ahmed, M., Lu, Y., Pan, S., Bo, W., Liu, Y.: Roformer: Enhanced transformer with rotary position embedding. *Neurocomputing* **568**, 127063 (2024)
54. Sun, C., Yuan, Z., Xu, K., Mai, L., N, S., Chen, S., Marina, M.K.: Learning high-frequency functions made easy with sinusoidal positional encoding. In: ICML (2024), <https://openreview.net/forum?id=qqPLOdkcrI>
55. Sun, L., Pan, J., Tang, J.: Shufflemixer: An efficient convnet for image super-resolution. *NeurIPS* **35**, 17314–17326 (2022)
56. Tian, Y., Chen, H., Xu, C., Wang, Y.: Image processing gnn: Breaking rigidity in super-resolution. In: CVPR. pp. 24108–24117 (2024)
57. Timofte, R., Agustsson, E., Van Gool, L., Yang, M.H., Zhang, L.: Ntire 2017 challenge on single image super-resolution: Methods and results. In: CVPRW. pp. 114–125 (2017)
58. Vaswani, A., Shazeer, N., Parmar, N., Uszkoreit, J., Jones, L., Gomez, A.N., Kaiser, Ł., Polosukhin, I.: Attention is all you need. *NeurIPS* **30** (2017)
59. Wang, H., Chen, X., Ni, B., Liu, Y., jinfan, L.: Omni aggregation networks for lightweight image super-resolution. In: CVPR (2023)
60. Wang, X., Xie, L., Yu, K., Chan, K.C., Loy, C.C., Dong, C.: BasicSR: Open source image and video restoration toolbox. <https://github.com/XPixelGroup/BasicSR> (2022)
61. Wu, H., Guo, M., Ma, Y., Sun, Y., Wang, J., Matusik, W., Long, M.: Flashbias: Fast computation of attention with bias. In: *NeurIPS* (2025), <https://openreview.net/forum?id=7L4NvUtZY3>
62. Xiong, W., Liu, J., Molybog, I., Zhang, H., Bhargava, P., Hou, R., Martin, L., Rungta, R., Sankararaman, K.A., Oguz, B., et al.: Effective long-context scaling of foundation models. In: NAACL. pp. 4643–4663 (2024)

63. Yang, A., Li, A., Yang, B., Zhang, B., Hui, B., Zheng, B., Yu, B., Gao, C., Huang, C., Lv, C., et al.: Qwen3 technical report. arXiv (2025)
64. Yun, S., Ro, Y.: Shvit: Single-head vision transformer with memory efficient macro design. In: CVPR. pp. 5756–5767 (2024)
65. Zamir, S.W., Arora, A., Khan, S., Hayat, M., Khan, F.S., Yang, M.H.: Restormer: efficient attention transformer for high-resolution image restoration. In: CVPR. pp. 5728–5739 (2022)
66. Zeyde, R., Elad, M., Protter, M.: On single image scale-up using sparse-representations. In: Curves and Surfaces: 7th International Conference, Avignon, France, June 24-30, 2010, Revised Selected Papers 7. pp. 711–730. Springer (2012)
67. Zhang, J., Zhang, Y., Gu, J., Zhang, Y., Kong, L., Yuan, X.: Accurate image restoration with attention retractable transformer. In: ICLR (2023)
68. Zhang, L., Li, Y., Zhou, X., Zhao, X., Gu, S.: Transcending the limit of local window: Advanced super-resolution transformer with adaptive token dictionary. In: CVPR. pp. 2856–2865 (2024)
69. Zhang, X., Zhang, Y., Yu, F.: Hit-sr: Hierarchical transformer for efficient attention image super-resolution. In: ECCV (2024)
70. Zhang, X., Zeng, H., Guo, S., Zhang, L.: Efficient long-range attention network for image super-resolution. In: ECCV. pp. 649–667. Springer (2022)
71. Zhang, Y., Li, K., Li, K., Wang, L., Zhong, B., Fu, Y.: Image super-resolution using very deep residual channel attention networks. In: ECCV. pp. 286–301 (2018)
72. Zhang, Y., Tian, Y., Kong, Y., Zhong, B., Fu, Y.: Residual dense network for image super-resolution. In: CVPR. pp. 2472–2481 (2018)
73. Zheng, M., Sun, L., Dong, J., Pan, J.: Smfanet: A lightweight self-modulation feature aggregation network for efficient image super-resolution. In: ECCV (2024)
74. Zhou, K., Lin, X., Lu, J.: Tsp-mamba: The travelling salesman problem meets mamba for image super-resolution and beyond. In: CVPR. pp. 28134–28143 (2025)
75. Zhou, K., Lin, X., Zhonghang, L., Han, X., Lu, J.: Ups: Unified projection sharing for lightweight single-image super-resolution and beyond. In: NeurIPS (2024)
76. Zhou, Y., Li, Z., Guo, C.L., Bai, S., Cheng, M.M., Hou, Q.: Srformer: Permuted self-attention for single image super-resolution. In: ICCV. pp. 12780–12791 (2023)

Rank-Factorized Implicit Neural Bias: Scaling Super-Resolution Transformer with FlashAttention

Supplementary Material

Supplementary material includes a summary of related work, implementation and training details, additional results on lightweight Super-Resolution (SR) tasks, comparisons of inference costs across FlashAttention implementations, and comparisons of inference costs across devices.

S1 Related Work

S1.1 Traditional CNNs

Early deep learning-based SR methods predominantly relied on a convolution operation, which is well suited for extracting local features from the input [13,14,33,34,50,71]. Motivated by prior findings that stacking small convolutions can gradually expand the effective receptive field while keeping the parameter count relatively modest [51], many convolution-based works adopted designs that heavily stack 3×3 convolutions. However, such designs only model long-range dependencies indirectly, which limits their ability to capture similar but spatially distant patterns [32]. Moreover, these stacked 3×3 convolutional structures often introduce large parameter counts, frequently leading to over-parameterization [44].

S1.2 Transformers

To address these limitations, Transformers [58], which leverage self-attention as a core operator, have garnered significant attention in SR tasks. By performing input-adaptive global feature aggregation, self-attention offers strong representational capacity and can potentially improve performance with fewer parameters and lower computational cost. Nevertheless, unlike many vision tasks that treat an image patch (e.g., 16×16) as a token, SR commonly operates at the pixel level and processes high-resolution inputs, making it difficult to apply vanilla self-attention directly due to its quadratic complexity. Therefore, many SR Transformers restrict self-attention to local windows to address the quadratic complexity of self-attention [35]. While this makes the computational cost more practical and manageable, it also limits long-range modeling capability. As a result, much recent effort has focused on expanding the receptive field while reducing the number of pixels involved in self-attention computation [5,7,8,32,48,67,76].

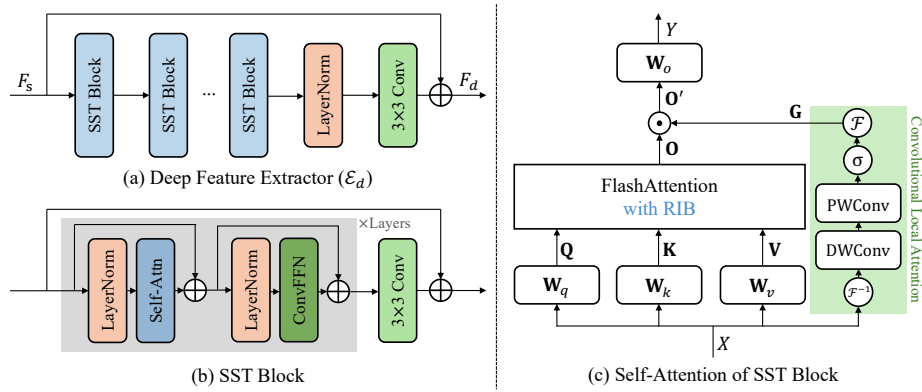


Fig. S1: Overall illustration for SST architecture.

S1.3 Alternative Operators

Another actively studied direction is to replace self-attention with sub-quadratic operators. Representative examples include proposing attention-like operators with sub-quadratic complexity [6, 9, 65, 68], adapting Mamba [19], which has attracted substantial interest in sequence/language modeling, to the SR domain [21, 22, 74], and integrating sparsification into self-attention [36, 40]. For lightweight SR, where efficiency under small model size is a primary goal, leveraging large-kernel convolutions [24, 29, 55, 73] and reducing the number of attention-map computations [45, 70, 75] have also been considered.

S1.4 Hardware-Efficient Acceleration Methods

However, most of the aforementioned approaches focus mainly on computational complexity and comparatively overlook memory efficiency. In practice, when data movement becomes the bottleneck, cutting floating-point operations (FLOPs) alone often fails to reduce latency and memory usage. For instance, self-attention repeatedly moves large $N \times N$ matrices (e.g., \mathbf{S} and \mathbf{P}) between HBM and SRAM during execution, which can incur substantial latency and memory overhead that FLOPs fail to account for. To directly mitigate this issue, FlashAttention [11, 12, 49] was introduced to reduce memory traffic while still computing exact attention, thereby significantly lowering latency and memory usage. Due to its practical impact, FlashAttention has been rapidly adopted across diverse Transformer applications, and is becoming a key ingredient for scaling Transformers in terms of both model size and sequence length. In SR, however, the relative position bias (RPB) that is crucial for performance [35, 47] is not compatible with the layouts supported by FlashAttention, making it difficult to leverage FlashAttention directly. Several works have attempted to resolve this limitation [30, 61]. Yet, FlashBias [61] suffers from severe performance degradation

Table S1: Network implementation details.

Methods	D	Blocks	Layers	Window Sizes	Heads	L	d_h	R	ConvFFN Exp.
SST-light	48	5	6	[8, 16, 32, 16, 32, 64]	3	10	32	[16, 16, 16, 24, 24, 24]	1.5
SST-light+	48	5	6	[16, 32, 48, 32, 48, 96]	3	10	32	[16, 16, 16, 24, 24, 24]	1.5
SST	180	6	6	[16, 32, 64, 16, 32, 64]	6	10	32	[18, 18, 18, 34, 34, 34]	1.25
SST+	180	6	6	[16, 32, 48, 32, 48, 96]	6	10	32	[18, 18, 18, 34, 34, 34]	1.25
SST-L	192	8	6	[16, 32, 64, 16, 32, 64]	6	10	32	[16, 16, 16, 32, 32, 32]	2
SST-L+	192	8	6	[16, 32, 48, 32, 48, 96]	6	10	32	[16, 16, 16, 32, 32, 32]	2

Table S2: Training configuration across our networks for $\times 2$ upscaling. For $\times 3$ and $\times 4$, we initialize from the weights of $\times 2$ and $\times 3$, respectively [28], and halve the number of iterations, learning rate, and schedule.

Methods	TrainingPatch	Dataset	BatchSize	Iteration	Optimizer	LR	Schedule ($\gamma = 0.5$)	Loss
SST-light	64 \times 64	DIV2K	64	500000	AdamW	5e-4	[250000, 400000, 450000, 475000, 490000]	L1Loss
SST-light+	96 \times 96	or DFLIP						
SST	64 \times 64	DF2K	32	500000	AdamW	5e-4	[250000, 400000, 450000, 475000, 490000]	L1Loss
SST+	96 \times 96							
SST-L	64 \times 64	DF2K	32	500000	AdamW	5e-4	[250000, 400000, 450000, 475000, 490000]	L1Loss
SST-L+	96 \times 96	or DFLIP						

when training models from scratch, and FlexAttention [15]-based implementations [30] rely on specific frameworks and low-level compilation, which increases system complexity and slows down training (please refer to Table 4 in the main manuscript).

S2 Implementation and Training Details

Our network follows the same overall architecture as the standard SR Transformer [32], and its detailed configuration is provided in Figure S1 and Table S1. On top of the window-based self-attention layer [32], we incorporate only two proposed components: the proposed Rank-factorized Implicit Neural Bias (RIB) and a convolutional local-attention module (CLA). We also adopt the ConvFFN introduced in prior work [76], setting the kernel size to 3 to strengthen high-frequency feature extraction. Inspired by previous work [69], we replace shifted windows with a cyclic window strategy, which periodically increases the window sizes. This design aims to extract multi-scale features while enabling more aggressive use of large windows. Among the RIB hyper-parameters (L, d_h, R), we set $L = 10$ following the ablation results in Table 5 in the main manuscript, and choose d_h and R empirically. In particular, for R , we select a value such that the dimensionality ($D + R$), after combining positional tokens with pixel tokens, is a multiple of 8. This allows us to match the FlashAttention layout without channel-wise zero padding. For our experiments, we use PyTorch version 2.9.1 and implement our method using the widely used BasicSR toolbox [60].

Table S3: Training/inference costs of attention variants on SST-L+. Training and inference costs are measured as detailed in Table 1.

Attention	Training		Inference	
	sec/step	memory	latency	memory
FlashAttention2 [11]	0.556	47.1GB	503.7ms	2825MB
FlashAttention3 [49]	0.479	47.1GB	455.7ms	2825MB

As shown in the training configuration in Table S2, our overall training setup is largely consistent with prior studies. However, to highlight our main focus on scalability, we additionally consider variants trained with larger patch sizes (e.g., 96×96) and variants trained on larger-scale datasets (e.g., DFLIP [1, 31, 42, 57]).

S3 Comparisons of Training and Inference Costs Across FlashAttention Implementations

In this section, we compare the training and inference costs across different FlashAttention implementations. We consider FlashAttention2 [11], which is widely used in practice, and FlashAttention3 [49], an improved version optimized for Hopper GPUs. As shown in Table S3, FlashAttention3 achieves a 20% faster training throughput and a 10% lower inference latency compared to FlashAttention2. These results suggest that as FlashAttention continues to improve, our approach can benefit from additional acceleration with only minor changes to the overall method.

S4 Comparisons of Inference Costs Across Devices

We then evaluate the inference efficiency of our approach against representative SR baselines [5, 21, 22, 36, 68] by measuring inference latency and memory usage on a range of GPUs. As summarized in Table S4, our SST variants consistently achieve substantially lower memory consumption and faster inference latency than competing methods across all tested devices, highlighting the practical efficiency of our FlashAttention-based implementation.

S5 Comparisons on CLA and PWConv

In this section, we compare CLA with the PWConv-only gating module proposed in [46] through qualitative visualizations. As shown in Figure S2, when the gating module relies only on PWConv, the self-attention output (**O**) is heavily influenced by local details, making it difficult to consistently capture repeated edge patterns. In contrast, when CLA is applied, the gating path (**G**) takes responsibility for modeling local details, allowing **O** to focus more stably and robustly on

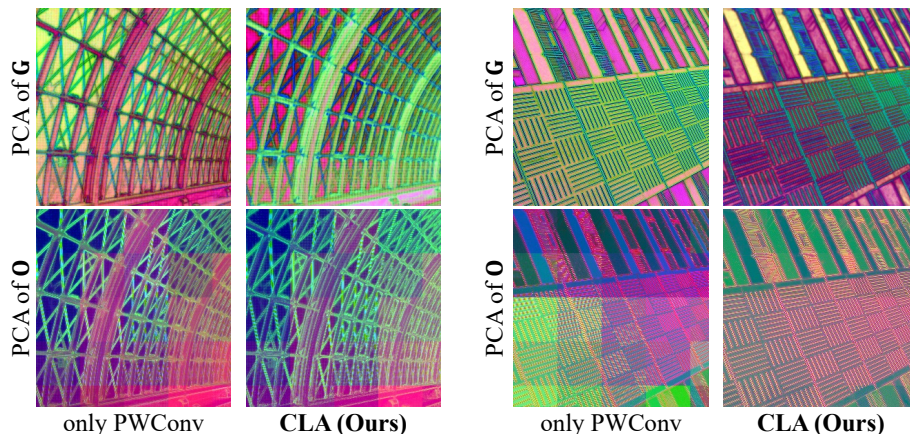


Fig. S2: PCA visualization of the gating coefficient (\mathbf{G}) and self-attention output (\mathbf{O}) under PWConv and our proposed Convolutional Local Attention (CLA). We visualize the first 64×64 window self-attention within the last SST block. To visualize the extracted features, we apply Principal Component Analysis (PCA) to reduce the channel dimension to three components and render them as RGB channels. Compared to PWConv-only variants, the self-attention layer with CLA is less affected by local textures and more robustly extracts structural features across the entire image.

repeated structures and edges. These results suggest that, unlike conventional PWConv-only gating modules originally introduced for NLP tasks, CLA better reflects the characteristics required for the SR domain. By incorporating convolution into the gating path, CLA helps self-attention capture repeated structures and edges more reliably, which in turn contributes to improved performance.

S6 Results on Lightweight Super-Resolution Tasks

Although our primary goal is to improve performance through scaling, the practical advantages of FlashAttention also make our approach highly effective in lightweight regimes. As shown in Tables S5 and S6, our method substantially improves both efficiency and reconstruction quality over existing RPB-based Transformer approaches. Notably, by leveraging scaling, our model achieves an impressive PSNR of 34.31 dB on Urban100 $\times 2$ even under a parameter budget of fewer than 1M parameters. These results highlight the practicality of our approach and demonstrate its potential for a wide range of applications.

Table S4: Latency and memory usage across GPUs. We use FlashAttention3 for an H200 GPU and FlashAttention2 for RTX4090 and A6000 GPUs. We report the measured median speed when restoring a 1280×720 image 10 times in FP32. Memory usage is measured using PyTorch’s `max_memory_allocated` function.

Methods	Scale	RTX4090		A6000		H200	
		latency	memory	latency	memory	latency	memory
HAT		1722.8ms	9047MB	3068.5ms	9047MB	709.7ms	9070MB
ATD		2665.8ms	6216MB	5064.8ms	6216MB	1266.8ms	6239MB
PFT		OOM	OOM	12990.1ms	28847MB	1920.8ms	28869MB
MambaIR		1570.8ms	6883MB	3349.4ms	7680MB	1043.8ms	7704MB
MambaIRV2	×2	3373.6ms	5749MB	9814.8ms	5792MB	2308.8ms	5816MB
SST		956.7ms	2675MB	1996.8ms	2675MB	428.9ms	2675MB
SST+		1046.0ms	2825MB	2125.3ms	2825MB	455.8ms	2825MB
SST-L		1439.2ms	2836MB	3051.8ms	2824MB	608.4ms	2824MB
SST-L+		1552.7ms	2990MB	3212.9ms	2990MB	644.9ms	2990MB
HAT		799.8ms	4040MB	1377.0ms	4040MB	317.8ms	4063MB
ATD		1210.3ms	2795MB	2220.6ms	2795MB	550.0ms	2819MB
PFT		2088.5ms	13525MB	4646.3ms	13525MB	892.7ms	13549MB
MambaIR		668.4ms	3125MB	1358.8ms	3458MB	465.1ms	3481MB
MambaIRV2	×3	1434.5ms	2589MB	4161.6ms	2632MB	1000.3ms	2655MB
SST		401.1ms	1296MB	739.2ms	1296MB	194.2ms	1296MB
SST+		446.8ms	1527MB	799.9ms	1527MB	207.1ms	1527MB
SST-L		609.1ms	1404MB	1112.5ms	1391MB	276.3ms	1391MB
SST-L+		667.0ms	1639MB	1191.6ms	1639MB	293.4ms	1639MB
HAT		510.8ms	2428MB	821.3ms	2428MB	195.8ms	2452MB
ATD		756.1ms	1692MB	1248.9ms	1692MB	339.0ms	1716MB
PFT		1237.4ms	7302MB	3168.1ms	7302MB	493.3ms	7326MB
MambaIR		356.5ms	1818MB	733.9ms	1990MB	269.7ms	2014MB
MambaIRV2	×4	848.9ms	1574MB	2188.1ms	1616MB	604.5ms	1640MB
SST		199.4ms	764MB	401.9ms	764MB	111.5ms	764MB
SST+		228.9ms	914MB	420.6ms	914MB	120.8ms	914MB
SST-L		308.6ms	907MB	556.3ms	919MB	158.3ms	941MB
SST-L+		346.0ms	1003MB	613.1ms	1003MB	170.4ms	1015MB

Table S5: Comparisons of lightweight SR methods trained on the DIV2K dataset. We reuse the statistics reported in prior work [30] and additionally include our results, measured following their procedure. The best result is bolded.

Method	Scale	Latency (ms)	Mem (MB)	#FLOPs (G)	#params (K)	PSNR / SSIM					
						Set5	Set14	B100	Urban100	Manga109	
SwinIR-lt [32]	×2	1409.8	1287	244.2	910	38.14/0.9611	33.86/0.9206	32.31/0.9012	32.76/0.9340	39.12/0.9783	
ELAN-lt [70]		94.5	887	203.1	621	38.17/0.9611	33.94/0.9207	32.30/0.9012	32.76/0.9340	39.11/0.9782	
OmniSR [59]		120.3	1031	194.5	772	38.22/0.9613	33.98/0.9210	32.36/0.9020	33.05/0.9363	39.28/0.9784	
SRFormer-lt [76]		1456.3	1184	236.3	853	38.23/0.9613	33.94/0.9209	32.36/0.9019	32.91/0.9353	39.28/0.9785	
ATD-lt [68]		733.5	2839	380.0	753	38.29/0.9616	34.10/0.9217	32.39/0.9023	33.27/0.9375	39.52/0.9789	
HiT-SRF [69]		268.1	1804	226.5	847	38.26/0.9615	34.01/0.9214	32.37/0.9023	33.13/0.9372	39.47/0.9787	
ASID-D8 [45]		131.2	999	190.5	732	38.32/0.9618	34.24/0.9232	32.40/0.9028	33.35/0.9387	- / -	
MambaIR-lt [22]		277.1	1695	334.2	905	38.13/0.9610	33.95/0.9208	32.31/0.9013	32.85/0.9349	39.20/0.9782	
MambaIRV2-lt [21]		580.4	2824	286.3	774	38.26/0.9615	34.09/0.9221	32.36/0.9019	33.26/0.9378	39.35/0.9785	
RDN [72]		279.3	2058	5096.2	22123	38.24/0.9614	34.01/0.9212	32.34/0.9017	32.89/0.9353	39.18/0.9780	
RCAN [71]		299.3	626	3529.7	15445	38.27/0.9614	34.12/0.9216	32.41/0.9027	33.34/0.9384	39.44/0.9786	
ESC [30]		120.9	831	592.0	947	38.35/0.9619	34.11/0.9223	32.41/0.9027	33.46/0.9395	39.54/0.9790	
SST-lt (Ours)		191.9	755	2057.6	893	38.35/0.9620	34.14/0.9227	32.41/0.9028	33.54/0.9399	39.48/0.9785	
SST-lt+ (Ours)		249.6	804	4903.3	893	38.35/0.9619	34.22/ 0.9232	32.44/0.9031	33.79/0.9417	39.59/0.9788	
SwinIR-lt [32]		×3	331.7	596	110.8	918	34.62/0.9289	30.54/0.8463	29.20/0.8082	28.66/0.8624	33.98/0.9478
ELAN-lt [70]			32.5	399	90.1	629	34.61/0.9288	30.55/0.8463	29.21/0.8081	28.69/0.8624	34.00/0.9478
OmniSR [59]	41.2		476	88.4	780	34.70/0.9294	30.57/0.8469	29.28/0.8094	28.84/0.8656	34.22/0.9487	
SRFormer-lt [76]	530.5		537	105.4	861	34.67/0.9296	30.57/0.8469	29.26/0.8099	28.81/0.8655	34.19/0.9489	
ATD-lt [68]	274.4		1258	168.0	760	34.74/0.9300	30.68/0.8485	29.32/0.8109	29.17/0.8709	34.60/0.9506	
HiT-SRF [69]	124.9		1464	101.6	855	34.75/0.9300	30.61/0.8475	29.29/0.8106	28.99/0.8687	34.53/0.9502	
ASID-D8 [45]	61.9		460	86.4	739	34.84/0.9307	30.66/0.8491	29.32/0.8119	29.08/0.8706	- / -	
MambaIR-lt [22]	109.3		760	148.5	913	34.63/0.9288	30.54/0.8459	29.23/0.8084	28.70/0.8631	34.12/0.9479	
MambaIRV2-lt [21]	259.0		1250	126.7	781	34.71/0.9298	30.68/0.8483	29.26/0.8098	29.01/0.8689	34.41/0.9497	
RDN [72]	146.5		985	2281.2	22308	34.71/0.9296	30.57/0.8468	29.26/0.8093	28.80/0.8653	34.13/0.9484	
RCAN [71]	85.1		560	1586.1	15629	34.74/0.9299	30.65/0.8482	29.32/0.8111	29.09/0.8702	34.44/0.9499	
ESC [30]	41.4		385	267.6	955	34.84/0.9308	30.74/0.8493	29.34/0.8118	29.28/0.8739	34.66/0.9512	
SST-lt (Ours)	69.2		359	954.1	900	34.79/0.9305	30.68/0.8489	29.31/0.8113	29.34/0.8748	34.55/0.9507	
SST-lt+ (Ours)	98.1		432	2397.7	900	34.80/ 0.9308	30.71/ 0.8495	29.34/0.8122	29.50/0.8774	34.67/0.9514	
SwinIR-lt [32]	×4		222.9	351	63.6	930	32.44/0.8976	28.77/0.7858	27.69/0.7406	26.47/0.7980	30.92/0.9151
ELAN-lt [70]			18.0	241	54.1	640	32.43/0.8975	28.78/0.7858	27.69/0.7406	26.54/0.7982	30.92/0.9150
OmniSR [59]		22.5	273	50.9	792	32.49/0.8988	28.78/0.7859	27.71/0.7415	26.64/0.8018	31.02/0.9151	
SRFormer-lt [76]		287.2	329	62.8	873	32.51/0.8988	28.82/0.7872	27.73/0.7422	26.67/0.8032	31.17/0.9165	
ATD-lt [68]		189.7	753	100.1	769	32.63/0.8998	28.89/0.7886	27.79/0.7440	26.97/0.8107	31.48/0.9198	
HiT-SRF [69]		82.1	1331	58.0	866	32.55/0.8999	28.87/0.7880	27.75/0.7432	26.80/0.8069	31.26/0.9171	
ASID-D8 [45]		61.8	265	49.6	748	32.57/0.8990	28.89/0.7898	27.78/0.7449	26.89/0.8096	- / -	
MambaIR-lt [22]		55.8	438	84.6	924	32.42/0.8977	28.74/0.7847	27.68/0.7400	26.52/0.7983	30.94/0.9135	
MambaIRV2-lt [21]		153.4	748	75.6	790	32.51/0.8992	28.84/0.7878	27.75/0.7426	26.82/0.8079	31.24/0.9182	
RDN [72]		66.0	791	1309.2	22271	32.47/0.8990	28.81/0.7871	27.72/0.7419	26.61/0.8028	31.00/0.9151	
RCAN [72]		52.2	540	917.6	15592	32.63/0.9002	28.87/0.7889	27.77/0.7436	26.82/0.8087	31.22/0.9173	
ESC [30]		21.9	215	149.2	968	32.68/0.9011	28.93/0.7902	27.80/0.7447	27.07/0.8144	31.54/0.9207	
SST-lt (Ours)		36.5	205	517.0	908	32.62/0.9007	28.93/0.7896	27.79/0.7446	27.12/0.8158	31.48/0.9200	
SST-lt+ (Ours)		53.0	253	1329.7	908	32.65/0.9003	28.94/0.7908	27.81/0.7454	27.23/0.8195	31.63/0.9219	

Table S6: Comparisons of lightweight SR methods trained on the DFLIP dataset. We reuse the statistics reported in prior work [30] and additionally include our results, measured following their procedure. The best result is bolded.

Method	Scale	Latency (MB)	Mem (mb)	#FLOPs (G)	#params (K)	PSNR / SSIM				
						Set5	Set14	B100	Urban100	Manga109
SRFormer-lt [76]	×2	1838.1	1184	236.3	853	38.24/0.9615	34.13/0.9218	32.42/0.9026	33.37/0.9386	39.36/0.9787
ATD-lt [68]		733.5	2839	380.0	753	38.29/0.9616	34.30/0.9230	32.43/0.9027	33.62/0.9401	39.60/0.9791
HiT-SRF [69]		268.1	1804	226.5	847	38.31/0.9616	34.31/0.9230	32.45/0.9031	33.58/0.9404	39.69/0.9793
ESC [30]		120.9	831	592.0	947	38.34/0.9618	34.42/0.9235	32.50/0.9036	33.86/0.9424	39.73/0.9795
SST-lt (Ours)		191.9	755	2057.6	893	38.39/ 0.9622	34.50/0.9245	32.50/0.9038	34.03/0.9436	39.72/0.9795
SST-lt+ (Ours)	249.6	804	4903.3	893	38.42/0.9622	34.62/0.9250	32.53/0.9042	34.31/0.9452	39.90/0.9798	
SRFormer-lt [76]	×3	668.3	537	105.4	861	34.67/0.9297	30.75/0.8484	29.30/0.8108	29.10/0.8701	34.26/0.9498
ATD-lt [68]		274.4	1258	168.0	760	34.71/0.9300	30.77/0.8493	29.33/0.8116	29.42/0.8743	34.61/0.9509
HiT-SRF [69]		124.9	1464	101.6	855	34.69/0.9298	30.81/0.8493	29.32/0.8115	29.28/0.8729	34.72/0.9511
ESC [30]		41.4	385	267.6	955	34.85/0.9312	30.97/0.8511	29.41/0.8135	29.70/0.8799	34.94/0.9525
SST-lt (Ours)		69.2	359	954.1	900	34.87/0.9310	30.92/0.8508	29.38/0.8131	29.74/0.8807	34.79/0.9520
SST-lt+ (Ours)	98.1	432	2397.7	900	34.93/0.9316	30.97/0.8514	29.41/0.8140	29.95/0.8840	34.99/0.9528	
SRFormer-lt [76]	×4	327.8	329	62.8	873	32.49/0.8993	28.89/0.7887	27.76/0.7429	26.90/0.8086	31.25/0.9189
ATD-lt [68]		189.7	753	100.1	769	32.52/0.8995	28.93/0.7896	27.79/0.7443	27.18/0.8150	31.47/0.9208
HiT-SRF [69]		82.1	1331	58.0	866	32.55/0.8997	28.96/0.7897	27.77/0.7443	27.07/0.8130	31.59/0.9208
ESC [30]		21.9	215	149.2	968	32.79/0.9025	29.06/0.7927	27.85/0.7466	27.45/0.8229	31.87/0.9239
SST-lt (Ours)		36.5	205	517.0	908	32.70/0.9017	29.03/0.7918	27.83/0.7459	27.41/0.8225	31.64/0.9224
SST-lt+ (Ours)	53.0	253	1329.7	908	32.71/0.9019	29.04/0.7921	27.86/0.7472	27.58/0.8270	31.92/0.9241	